



Structured Jets and X-Ray Plateaus in Gamma-Ray Burst Phenomena

Gor Oganessian^{1,2,3} , Stefano Ascenzi^{1,3} , Marica Branchesi^{1,2,3} , Om Sharan Salafia⁴ , Simone Dall’Osso¹, and Giancarlo Ghirlanda^{4,5}

¹ Gran Sasso Science Institute, Viale F. Crispi 7, I-67100, L’Aquila (AQ), Italy; gor.oganessian@gssi.it

² INFN—Laboratori Nazionali del Gran Sasso, I-67100, L’Aquila (AQ), Italy

³ INAF—Osservatorio Astronomico d’Abruzzo, Via M. Maggini snc, I-64100 Teramo, Italy

⁴ INAF—Osservatorio Astronomico di Brera, via Emilio Bianchi 46, I-23807 Merate (LC), Italy

⁵ INFN—Milano Bicocca, Piazza della Scienza 3, I-20123, Milano, Italy

Received 2019 April 18; revised 2020 March 18; accepted 2020 March 19; published 2020 April 20

Abstract

The first multi-messenger detection of a binary neutron star merger, GW170817, brought to the forefront the structured jet model as a way to explain multiwavelength observations taken more than a year after the event. Here, we show that the high-latitude emission from a structured jet can naturally produce an X-ray plateau in gamma-ray burst (GRB) light curves, independent of the radiation from an external shock. We calculate the radiation from a switched-off shell featuring an angular structure in both its relativistic bulk motion and intrinsic brightness. Our model is able to explain the shallow decay phase (plateau) often observed in GRB X-ray light curves. We discuss the possible contribution of the structured jet high-latitude emission to other distinctive features of GRB X-ray light curves, and its capability to explain the chromatic optical/X-ray light-curve properties.

Unified Astronomy Thesaurus concepts: [High energy astrophysics \(739\)](#); [Burst astrophysics \(187\)](#); [Gamma-ray bursts \(629\)](#)

1. Introduction

The follow up of gamma-ray bursts (GRBs) by the X-ray Telescope (XRT; 0.3–10 keV) on board the Neil Gehrels Swift Observatory (Swift, hereafter; Gehrels et al. 2004) has revealed a rich morphology and diversity in their X-ray counterparts. However, systematic studies of the X-ray light curves have identified a canonical behavior characterized by the presence of an early steep temporal decay, often followed by a shallow phase at nearly constant flux eventually turning into the characteristic temporal decay expected from an external shock (Nousek et al. 2006; Zhang et al. 2006).

Typically, the steep decay phase ($F_\nu \propto t^{-\alpha_1}$ with $3 \leq \alpha_1 \leq 5$) lasts up to $\sim 10^2$ – 10^3 s (Tagliaferri et al. 2005; O’Brien et al. 2006). The shallow decay phase (or “plateau,” $F_\nu \propto t^{-\alpha_2}$ with $\alpha_2 \sim 0.5$ or shallower) can extend up to $\sim 10^4$ – 10^5 s, and it is present in a good fraction of GRBs (Nousek et al. 2006; Zhang et al. 2006; Liang et al. 2007; Willingale et al. 2007). Later, the evolution of the X-ray light curve transitions to a more “canonical” decay ($F_\nu \propto t^{-\alpha_3}$, with $\alpha_3 \sim 1$ – 1.5), sometimes showing a further steepening on timescales of a few days. While α_3 is consistent with the temporal slope expected in the standard afterglow model (Sari et al. 1998), the steep decay and the plateau phases call for a different interpretation.

The initial steep decay phase observed by XRT is often modeled as high-latitude emission (e.g., Liang et al. 2006), i.e., the radiation received from larger angles relative to the line of sight, when the prompt emission from a curved surface is switched off (Fenimore et al. 1996). It was shown that high-latitude emission from a spherical surface has a power-law decay $F_\nu \propto t^{-(\hat{\beta}+2)}$, where $\hat{\beta}$ is the slope of the emitted spectrum, typically modeled as a simple power law, $F_\nu \propto \nu^{-\hat{\beta}}$ (Kumar & Panaitescu 2000). Different modifications of the standard high-latitude emission have been considered in previous studies. They include the effects of a finite cooling time (Qin 2008), a non-power-law input spectrum (Zhang et al.

2009), time-dependent bulk motion (Uhm & Zhang 2015), a finite size of the emitting shell with multi-pulse contributions (Genet & Granot 2009), an off-axis observer (Lin et al. 2018), and inhomogeneities of the relativistic jet (Dyks et al. 2005; Yamazaki et al. 2006; Takami et al. 2007). While these studies were focused on the effects of jet structure, the attention was restricted to the steep decay phase.

The plateau phase instead is usually explained by introducing nontrivial modifications of the standard afterglow theory. The proposed solutions include scenarios with time-varying microphysical parameters of the external shock (Ioka et al. 2006), long-lived reverse shocks (Genet et al. 2007; Uhm & Beloborodov 2007), delayed afterglow radiation from an inhomogeneous jet (Eichler & Granot 2006; Toma et al. 2006), afterglow radiation in the thick-shell model (Leventis et al. 2014), baryon loading into the external shock from the massive outer shell (Duffell & MacFadyen 2015), delayed onset of the afterglow emission (Kobayashi & Zhang 2007), two-component jet model (Jin et al. 2007), photospheric emission from a long-lasting outflow (Beniamini & Mochkovitch 2017), or possible emission prior to the main burst (Yamazaki 2009). Also, prompt emission scattered by dust grains (Shao & Dai 2007) and late-time prompt emission originating from less powerful shells with relatively smaller bulk Lorentz factors (Ghisellini et al. 2007) were proposed as alternative models.

However, the model with the largest consensus considers additional energy injection to the external decelerating shock (Rees and Mészáros 1998; Granot & Kumar 2006; Nousek et al. 2006; Zhang et al. 2006). The additional energy would prevent the blast wave from decelerating, thus avoiding the typical afterglow decay, $F \propto t^{-1}$. The plateau phase, observed up to several $\times 10^4$ s requires long-lasting activity of the central engine, which can be provided either by the long-term evolution of the accretion disk around a black hole (Kumar & McMahon 2008; Cannizzo & Gehrels 2009; Lindner et al.

2010) or by the spin-down power released by a newly born millisecond spinning and highly magnetized neutron star (Dai & Lu 1998a, 1998b; Zhang and Mészáros 2001; Dai 2004; Yu et al. 2010; Dall’Osso et al. 2011; Metzger et al. 2011).

Despite many theoretical efforts to explain the origin of the X-ray plateau (with or without energy injection), there is not a clear consensus on its origin (see Kumar & Zhang 2015 for a review). The main difficulty of these models is the lack of a robust explanation for the observed chromatic behavior of X-ray and optical afterglow light curves (see Fan & Piran 2006).

The structured jet, i.e., a jet with an angular profile in both the bulk Lorentz factor and luminosity (Dai & Gou 2001; Lipunov et al. 2001; Rossi et al. 2002; Zhang and Mészáros 2002), has been invoked to explain the multi-wavelength observations of GRB170817A/GW170817 taken over one year (e.g., Ghirlanda et al. 2019). Moreover, the structured jet has been shown to provide a natural explanation for the luminosity function of GRBs (Pescalli et al. 2015). In this work, we test the idea that, along with the steep decay, the high-latitude emission during the prompt phase from a structured jet can produce the plateau observed in the light curve at late times. Qualitatively, the decreasing relativistic beaming of the emission at higher latitudes leads to a shallower light curve with respect to the uniform jet, for which the bulk Lorentz factor is constant throughout the emitting surface. Furthermore, the latitude-structured bulk motion results in an oblate geometry of the emitting surface that further extends the high-latitude emission in time. To be more specific, we seek long-lasting ($\sim 10^2$ – 10^4 s) flat segments in the light curves from high-latitude emission arising after 10^2 – 10^3 s when the emitting source is switched off.

2. High-latitude Emission from a Structured Jet

We assume an expanding shell in vacuum. As a result of prior interaction with a surrounding medium (the envelope of the progenitor star or the ejecta cloud of the progenitor neutron star merger), different parts of the shell move with different velocities. We assume axisymmetry of the velocity relative to the azimuthal angle (in spherical coordinates) and that the observer is perfectly aligned with the center of the shell. At a given time in the rest frame, radiation is produced throughout the entire shell with an infinitesimally short duration.

The adopted model is sketched in Figure 1: we consider and compare the Uniform Jet model (red curve) with the Structured Jet model (blue curve). In the uniform jet model, the Lorentz factor is constant along the emitting surface, which is a portion of a sphere. In the structured jet case, instead, the Lorentz factor $\Gamma(\theta)$ decreases with the angular distance from the jet axis, θ .

The observed flux then depends on the Doppler factor $\mathcal{D}(\theta) = 1/[\Gamma(\theta)(1 - \beta(\theta)\cos\theta)]$ where $\beta = v/c$. In the uniform jet model (red curve in Figure 1), the bulk Lorentz factor is constant throughout the shell. This results in a beaming cone with the same angular size $\sim 1/\Gamma$ at each θ . With increasing time, the observer progressively receives further out of the beaming cone coming from annuli located at larger angular distances θ , causing the monotonic decay of the received flux. In the structured jet model (blue curve in Figure 1), the elongated geometry of the emitting surface causes a slower increase of θ , which in turn increases the duration of the high-latitude emission. Moreover, the beaming cones corresponding to larger θ have increasingly wide beaming angles.

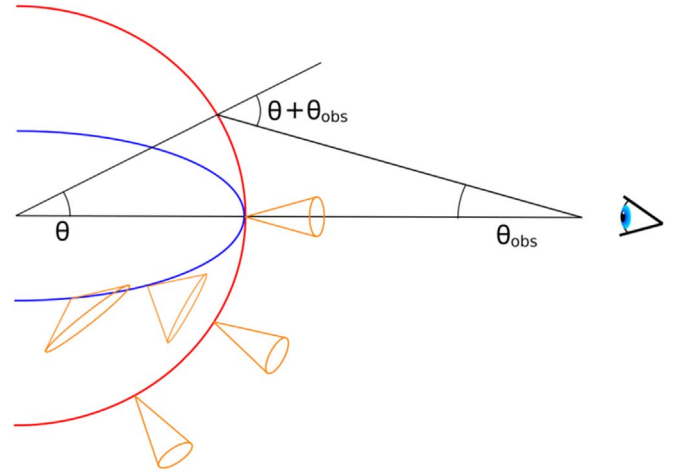


Figure 1. Spherical (red) and structured (blue) emitting surfaces corresponding to the uniform jet and the structured jet, respectively. For the uniform jet, Γ is constant all over the surface, while in the structured jet, there is an angular dependence that results in the widening of the emitted radiation beaming cone. At a fixed θ , the travel time of photons in the structured jet is longer than in the spherical case. We assume $\theta + \theta_{\text{obs}} \approx \theta$, i.e., we consider distant observers.

With the assumption that each patch of the shell moves at a constant velocity, we derive the relation between the observed time t_{obs} and the angle of the jet $\theta(t_{\text{obs}})$ from which radiation is received at t_{obs} :

$$\frac{1}{\beta(0)} - \frac{\beta(\theta)}{\beta(0)} \cos\theta = \frac{ct_{\text{obs}}}{R_0} \quad (1)$$

where R_0 is the radius of the emitting surface at $\theta = 0$. The first photon is assumed to arrive from the origin of a GRB.

The observed specific flux is given by the intrinsic spectral shape $S(\nu')$ and the comoving time-integrated surface brightness $\epsilon(\theta)$:

$$F_\nu(t_{\text{obs}}) \propto \mathcal{D}^2(\theta) S(\nu') \epsilon(\theta) \frac{\beta^2(\theta)}{\Gamma(\theta)} \frac{\sin\theta \cos\theta d\theta}{dt_{\text{obs}}} \Big|_{\theta(t_{\text{obs}})} \quad (2)$$

where the observer frequency is $\nu = \mathcal{D}(\theta)\nu'$ (primed quantities are in the comoving frame). The detailed derivation of Equation (2) is given in the Appendix.

We assume that the intrinsic spectral shape $S(\nu')$ is angle-independent, and we normalize it to 1. For both the uniform jet and the structured jet, the observed flux can be computed by Equation (2), once the bulk Lorentz factor $\Gamma(\theta)$, the comoving brightness $\epsilon(\theta)$, and the intrinsic spectral shape $S(\nu')$ are specified. For a uniform jet, the brightness is constant throughout the surface.

It is worth noticing that the expression in Equation (2) integrates over equal arrival time rings and, thus, represents a single-dimension approximation for the computation of the flux. Considering a finite time duration of the pulse would require integration over equal arrival time surfaces (e.g., see Fenimore et al. 1996; Dermer 2004; Genet & Granot 2009; Salafia et al. 2016). The latter results in second-order contributions to the observed flux due to the finite width of the emitting surface, and it is neglected here.

2.1. The Gaussian Structured Jet

We adopt a Gaussian jet structure for $\Gamma(\theta)$ and $\epsilon(\theta)$, with the same form as in Salafia et al. (2015):

$$\begin{aligned}\epsilon(\theta) &= \epsilon_c e^{-(\theta/\theta_c)^2} \\ \Gamma(\theta) &= 1 + (\Gamma_c - 1) e^{-(\theta/\theta_\Gamma)^2}\end{aligned}\quad (3)$$

where ϵ_c and Γ_c are the comoving core brightness and the bulk Lorentz factor at $\theta = 0$, while θ_c and θ_Γ are the jet scaling factors.⁶ To compute the observed flux density $F_\nu(t_{\text{obs}})$, we adopt a power-law spectral shape $S(\nu') \propto \nu'^{-\hat{\beta}}$. The shape of the spectrum influences the temporal behavior of the high-latitude emission since the comoving energy range is blue-shifted by $\mathcal{D}(\theta)$, which introduces a spectral dependence in Equation (2).

The shape of the light curve in the Gaussian jet structure case is defined by five parameters: R_0 , Γ_c , θ_c , θ_Γ , and the spectral slope $\hat{\beta}$. We compute a sequence of light curves with variable parameter sets. For simplicity, we assume that θ_c is equal to θ_Γ , and set $\hat{\beta}$ to 1.0, which is the average observed spectral index in the plateau phase (Liang et al. 2007). We notice that flat portions of the light curves can be achieved at relatively late times $t_{\text{obs}} > 10^2$ s for $R_0 \geq 10^{15}$ cm, $\Gamma_c \geq 100$ and $\theta_{c,\Gamma} \geq 3^\circ$.

In Figure 2, we show the time evolution of θ , \mathcal{D} , and the corresponding light curves for fixed $R_0 = 10^{15}$ cm and $\Gamma_c = 100$, and three different values of $\theta_{c,\Gamma}$. The result in the uniform jet case is also reported for reference (solid orange line). The evolution of the polar angle θ from where the observer receives photons at a given time is shallower for the structured jet (panel A), as a consequence of the oblateness of the emitting surface: the narrower the jet, the longer the time travel difference between photons emitted at different angles. Therefore, the observed timescale of high-latitude emission is longer than in the uniform jet case. The time evolution of the Doppler factor is affected both by $\theta(t_{\text{obs}})$ and $\Gamma(\theta)$ (panel B). On one hand, the decrease of $\Gamma(\theta)$ with time increases \mathcal{D} , and on the other hand, the increase of θ with time reduces \mathcal{D} . As a result, there is a time interval where \mathcal{D} is roughly constant or slightly increasing, while $\epsilon(\theta)$ is still not decreasing much: this gives rise to the plateau in the light curve (panel C). The deviation of the Gaussian jet structure case from the uniform jet case happens essentially at the time when the observer sees the radiation coming from the core border, i.e., when $\theta = \theta_{c,\Gamma}$. While we have fixed $\hat{\beta}$ to 1.0 and R_0 to 10^{15} cm, it is worth mentioning the effects of varying these parameters. Softer spectra result in steeper decays (as expected in the standard high-latitude emission) and fainter plateaus. The influence of the size of the jet on the high-latitude emission light curve is straightforward: smaller R_0 causes an earlier steep decay.

The dependence of the high-latitude emission on the bulk Lorentz factor (panel D) shows that the light curves with larger Γ_c present a bump at $t_{\text{obs}} > t_c$. This re-brightening can be interpreted as follows: given equal $\theta_{c,\Gamma}$, cases with higher Γ_c are characterized by a higher beaming of radiation for $\theta < \theta_{c,\Gamma}$. Approaching $\theta_{c,\Gamma}$, a larger fraction of radiation will be beamed out from the observer, with respect to the low Γ_c case. So, we can expect a higher flux when Γ_c is lower. For $\theta \gg \theta_\Gamma$, instead, the steep decrease of $\Gamma(\theta)$ results in a widening of the beaming

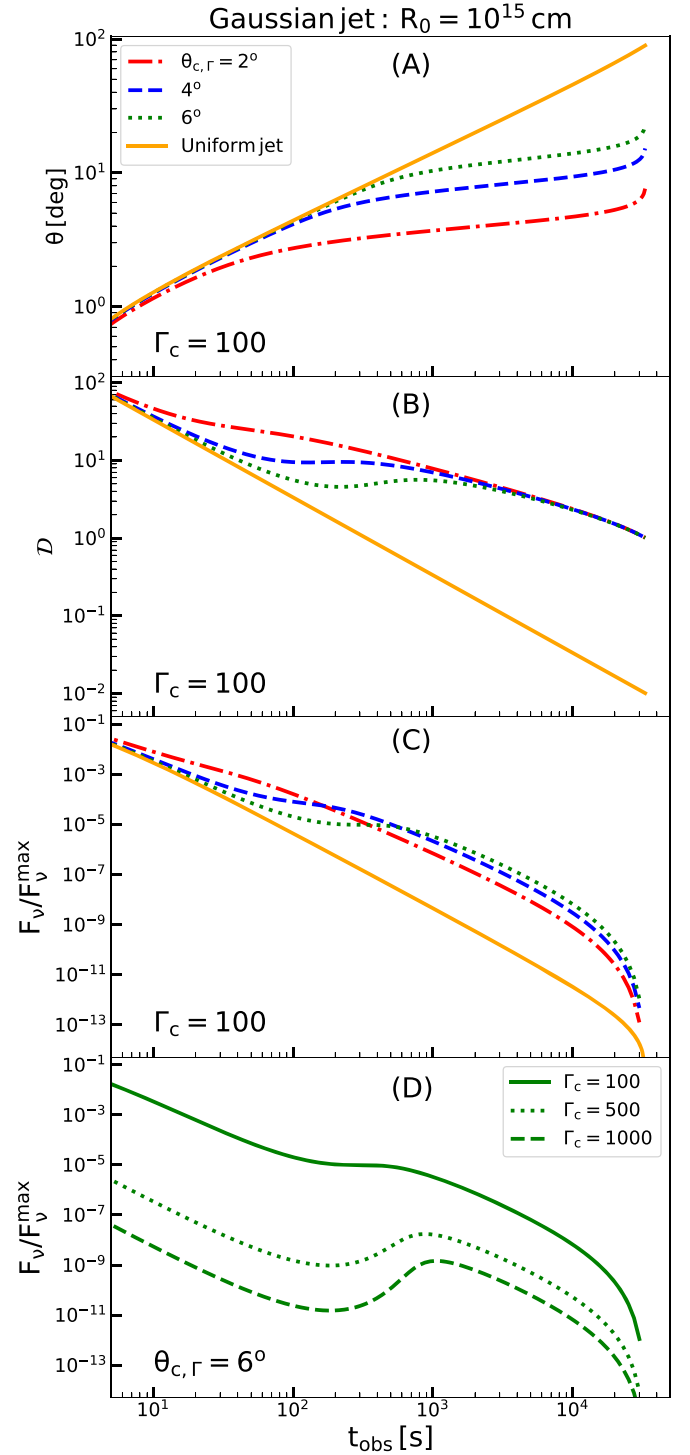


Figure 2. Time evolution of the polar angle θ of the jet from where radiation is observed (panel A), the corresponding Doppler factor \mathcal{D} (panel B), and the high-latitude emission light curves ($\hat{\beta} = 1$, panel C) for the Gaussian jet structure. The colors separate cases with different angular sizes of the jet for the same radial size $R_0 = 10^{15}$ cm and central bulk Lorentz factor $\Gamma_c = 100$. The solid orange lines represent the uniform jet. The dependence of the light curves on the central bulk Lorentz factor Γ_c is shown in panel D ($\theta_{c,\Gamma}$ is fixed to 6°).

angle, which is similar for both the high and low Γ_c cases. Therefore, in this picture, the flux emitted by $\theta \gg \theta_\Gamma$ is almost the same for high and low Γ_c , while the flux emitted for $\theta \sim \theta_\Gamma$ will suffer a beaming-driven suppression in the high Γ_c case. As a consequence, the light curve characterized by high Γ_c will

⁶ While the jet structure in Salafia et al. (2015) is adopted for the lab-frame energy per solid angle, we use it here for the comoving brightness.

show the re-brightening, which is, however, the consequence of the suppression of the flux at earlier times.

The comoving brightness structure of the jet, $\epsilon(\theta)$, additionally suppresses the light-curve intensity. The dependence of the light-curve shape on $\epsilon(\theta)$ is much weaker than the dependence on \mathcal{D} . However, once the Doppler factor drops below 1, the emission becomes de-beamed and the plateau ends. The later very sharp drop is caused by having reached the edge of the jet.

2.2. Power-law Structured Jet

We compute high-latitude emission from the power-law jet structure for $\epsilon(\theta)$ and $\Gamma(\theta)$ adopted from Salafia et al. (2015):

$$\epsilon(\theta) = \begin{cases} \epsilon_c & \theta \leq \theta_c \\ \epsilon_c(\theta/\theta_c)^{-k} & \theta > \theta_c \end{cases}$$

$$\Gamma(\theta) = \begin{cases} \Gamma_c & \theta \leq \theta_\Gamma \\ 1 + (\Gamma_c - 1)(\theta/\theta_\Gamma)^{-k} & \theta > \theta_\Gamma \end{cases} \quad (4)$$

where ϵ_c and Γ_c are the comoving brightness and the bulk Lorentz factor, respectively, at $\theta = 0$, θ_c and θ_Γ are the jet scaling factors, and k is the slope of the power-law tail, i.e., the steepness of the jet structure.

We compute the observed flux density $F_\nu(t_{\text{obs}})$ using a power-law spectrum $S(\nu') \propto \nu'^{-\beta}$ with $\beta = 1.0$. In Figure 3, we show the time evolution of θ (panel A), \mathcal{D} (panel B), and the corresponding light curves for $R_0 = 10^{15}$ cm, $\Gamma_c = 100$, $k = 2$, and $\theta_{c,\Gamma}$ varying in the range between 2° and 6° (panel C). We also present high-latitude emission from the uniform jet (solid orange line). One can notice that the rise of θ is faster compared to the Gaussian jet structure case. This is simply due to the shallower angle dependence of $\Gamma(\theta) \propto \theta^{-2}$ than in Gaussian jet structure. The Doppler factor deviates from the uniform jet case at times $t_{\text{obs}} > t_c$ (post-core): the smaller the core size of the jet, the earlier the slowing down of the $\mathcal{D}(t_{\text{obs}})$ variation. The major difference of $\mathcal{D}(t_{\text{obs}})$ compared to the Gaussian jet structure case is that the post-core temporal decay is monotonic, contrary to the ‘‘bumpy’’ trend of the Gaussian jet structure (see panel B of Figure 2). The plateau phase is more prominent and longer (up to few 10^4 s) in the power-law jet structure case. The fast rise of $\theta(t_{\text{obs}})$ results in the sharp decay phase at the end of the plateau.

We show the high-latitude emission dependence on Γ_c in panel D. One can notice that the plateau phase is flatter with an increase of Γ_c . The flat and long plateau is provided by the shallow jet structure, i.e., $k = 2$, which causes an extremely fast rise of $\theta(t_{\text{obs}})$.

The increase of k results in re-brightening of the light curve (see Figure 4). The origin of the re-brightening for higher k is due to the fact that a steeper jet structure leads to a faster widening of the beaming angle. This results in a higher fraction of radiation reaching the observer at post-core time.

3. Testing Predictions of the High-latitude Emission Model

In order to test our model’s ability to match the temporal properties of the observed X-ray plateaus, we compare our model predictions with the observed X-ray light curves.

We compare our model calculations with the observed X-ray light curves of GRB 061121 (Golenetskii et al. 2006; Page et al. 2006) and GRB 100906A (Golenetskii et al. 2010;

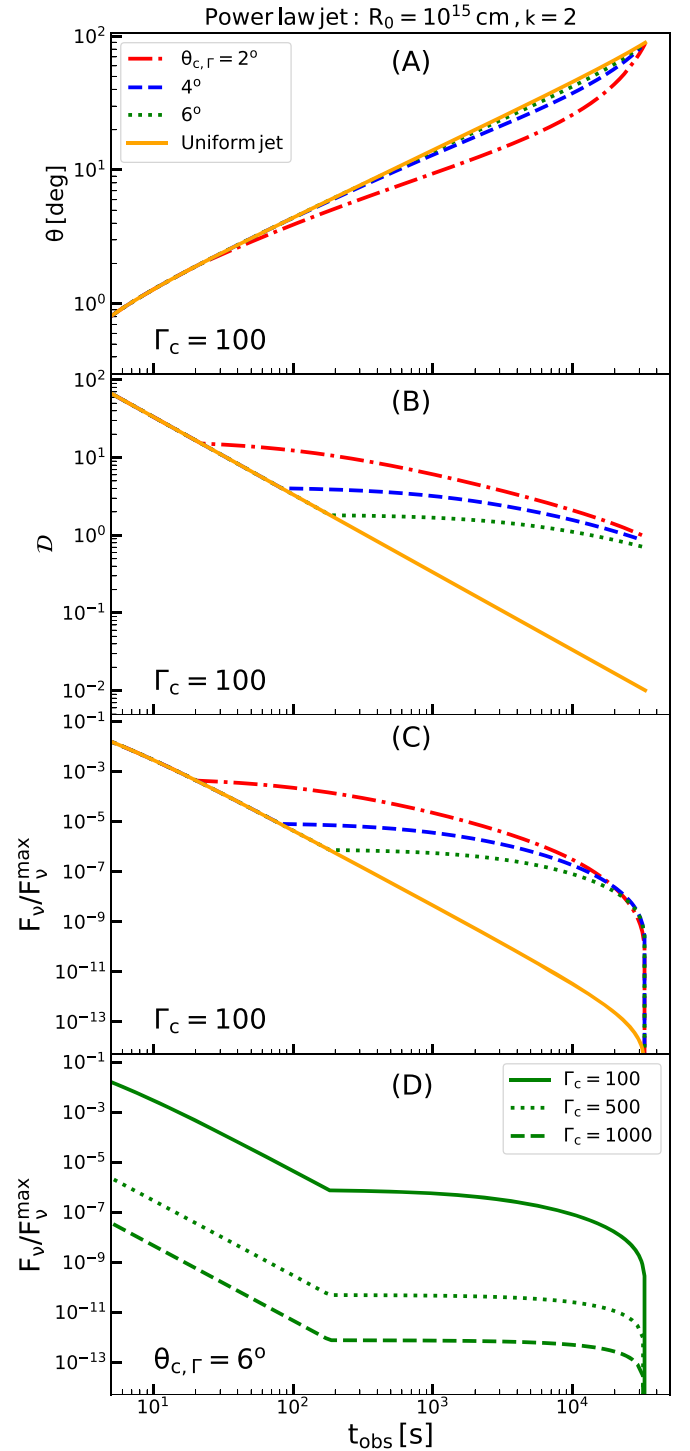


Figure 3. Time evolution of the polar angle θ of the jet from where radiation is observed (panel A), the corresponding Doppler factor \mathcal{D} (panel B), and the high-latitude emission light curve ($\beta = 1$, panel C) for the power-law structured jet. The colors show cases with different angular sizes of the jet for the same radial size $R_0 = 10^{15}$ cm, central bulk Lorentz factor $\Gamma_0 = 100$, and power-law index $k = 2$. The solid orange lines represent the uniform jet. The dependence of the light curves on the central bulk Lorentz factor Γ_c is shown in panel D ($\theta_{c,\Gamma}$ is fixed to 6°).

Markwardt et al. 2010). The choice of these particular GRBs is motivated by the following requirements:

1. Presence of the fast decay and plateau phases in the X-ray light curve.

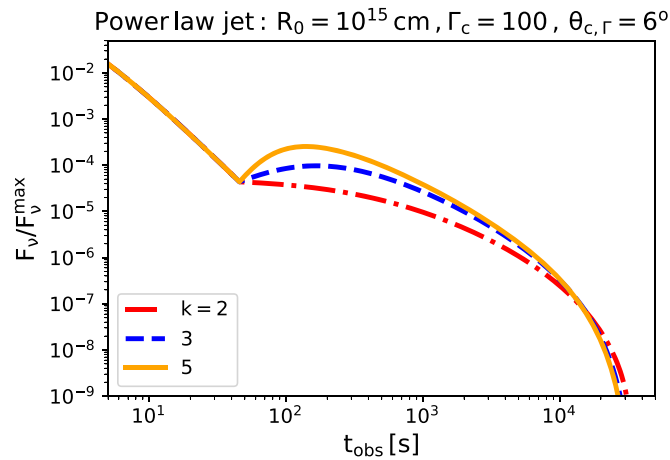


Figure 4. The high-latitude emission light curves for the power-law structured jet. The colors show cases with different power-law indices k .

2. Relatively bright GRB in order to best meet the assumption of an “on-axis” observer.

3.1. High-latitude Emission Against X-Ray Data

For each time-bin, we downloaded XRT spectra from the UK Swift Science Data Centre at the University of Leicester.⁷ We then fitted each of time-resolved XRT spectra using XSPEC (v12.10.0c) by a power-law model taking into account Galactic and intrinsic metal absorption (Wilms et al. 2000). The Galactic absorption has been estimated from Kalberla et al. (2005) while the intrinsic column density of hydrogen is a free parameter of the fit. We derived the unabsorbed flux for all time-resolved spectra and then built the final light curves of GRB 061121 and GRB 100906A shown in Figure 5. The peak times of the main prompt pulse for GRB 061121 and GRB 100906A occur at $t_0 \sim 74$ s and $t_0 \sim 7$ s, respectively. This is chosen as time zero for our model, i.e., we assume the emitting source is switched off at t_0 . Therefore, we changed the reference times for the light curves correspondingly. For the initial 10 s of GRB 100906A, which lacks the XRT data, we estimated the soft X-ray flux by extrapolating the Swift/BAT spectra to the XRT energy range.⁸

In order to produce the high-latitude emission light curve, we assume a synchrotron spectrum of the prompt emission pulse. Synchrotron has been proposed as the dominant radiation mechanism responsible for GRB prompt emission (Katz 1994; Rees & Meszaros 1994; Kobayashi et al. 1997; Sari & Piran 1997; Daigne & Mochkovitch 1998). In a few GRBs, prompt spectra were successfully fitted assuming a single-component synchrotron emission from a nonthermal population of electrons (e.g., Tavani 1996; Lloyd & Petrosian 2000; Zhang et al. 2016, 2018). Recent studies of the broadband GRB spectra have shown the ability of the synchrotron model *alone* to account for the entire prompt emission spectrum once *the cooling of electrons is taken into account* (Oganesyan et al. 2017, 2018, 2019; Ravasio et al. 2018, 2019). Motivated by these recent results, we adopt a double broken power-law model (2BPL) with synchrotron slopes to model high-latitude emission from the prompt emission pulse. The photon indices

below and above the low-energy break at E_{break} are $\alpha_1 = -2/3$ and $\alpha_2 = -1.5$, which correspond to spectral indices $\beta_1 = -1/3$ and $\beta_2 = 0.5$ in the $F_\nu \propto \nu^{-\beta}$ representation.

The spectrum around the peak time of the prompt pulse (t_0) of GRB 061121 is best fitted with $E_{\text{break}} \sim 3$ keV (Oganesyan et al. 2017). We use this value as input for modeling the high-latitude emission in the XRT spectral range. The corresponding break energy in the comoving frame is then $E_{\text{break}}/D(\theta = 0)$. Furthermore, we assume the peak energy (corresponding to the break at higher energy in the 2BPL model) $E_{\text{peak}} > 150$ keV since it is not constrained by the BAT data. However, we verified that its exact value does not affect the X-ray light curve at the observed time of the plateau. To reproduce the fast decay and the plateau phase observed in the X-ray emission (at 0.5–10 keV) of GRB 061121 using the high-latitude emission model, we adopt a power-law jet structure with $\Gamma_c = 250$, $R_0 = 3 \times 10^{16}$ cm, $\theta_c = \theta_\Gamma = 1^\circ$, and $k = 2$ (the red line in the left panel of Figure 5). The final model is represented in the reference time \hat{t}_{obs} of the first photon arriving from the head of the jet, i.e., $\theta = 0$ (see the Appendix).

The high-latitude model for GRB 100906A is obtained with $\Gamma_c = 160$, $R_0 = 9 \times 10^{15}$ cm, $\theta_c = \theta_\Gamma = 2^\circ$, and $k = 2$ (the right panel of Figure 5). We adopted a peak energy of the BAT spectrum of ~ 100 keV (Barthelmy et al. 2010), placing the break energy at sub-keV energy range. One can notice an X-ray flare at ~ 120 s during which the high-latitude emission is well below the X-ray flux.

These examples illustrate the role of high-latitude emission in shaping GRB light curves: this additional component of the prompt emission turns out to be particularly important in the X-ray range to naturally produce a steep decay followed by a longer-lasting plateau as a consequence of a generic jet structure. The high-latitude emission model requires large radii of the prompt emission zone $\sim 10^{16}$ cm. Such radii are expected in the synchrotron-dominated models for the prompt emission (Kumar & McMahon 2008; Beniamini & Piran 2013; Beniamini et al. 2018). Additional constraints on the jet properties would also require a comprehensive consideration of the observed GRB luminosity functions (see Beniamini & Nakar 2019).

There are observational indications from the temporal and spectral behavior of multiwavelength data that optical and X-ray emission could arise from different emission regions (e.g., Li et al. 2015). This is addressed below.

3.2. Multiwavelength Modeling Including the Forward Shock Contribution

Here, we investigate how accurately our model predictions can describe the multiwavelength emission of the GRB 061121 and GRB 100906A including the forward shock emission expected from the structured jet. We assume the model of Salafia et al. (2019b), where the afterglow emission from the forward shock accounts for the jet structure. The model based on standard afterglow concepts (Meszaros & Rees 1993, 1997; Sari et al. 1998) accounts for synchrotron emission from the external forward shock and includes the effect of radiative cooling and of synchrotron self-absorption. The shock dynamics is computed throughout its evolution, from coasting to the self-similar phase (Blandford & McKee 1976), down to the nonrelativistic phase. The emission at a given observed time is computed on the relevant equal-arrival-time surface (EATS), assuming that the emitting region (i.e., the shocked

⁷ https://www.swift.ac.uk/xrt_spectra/

⁸ https://www.swift.ac.uk/burst_analyser/

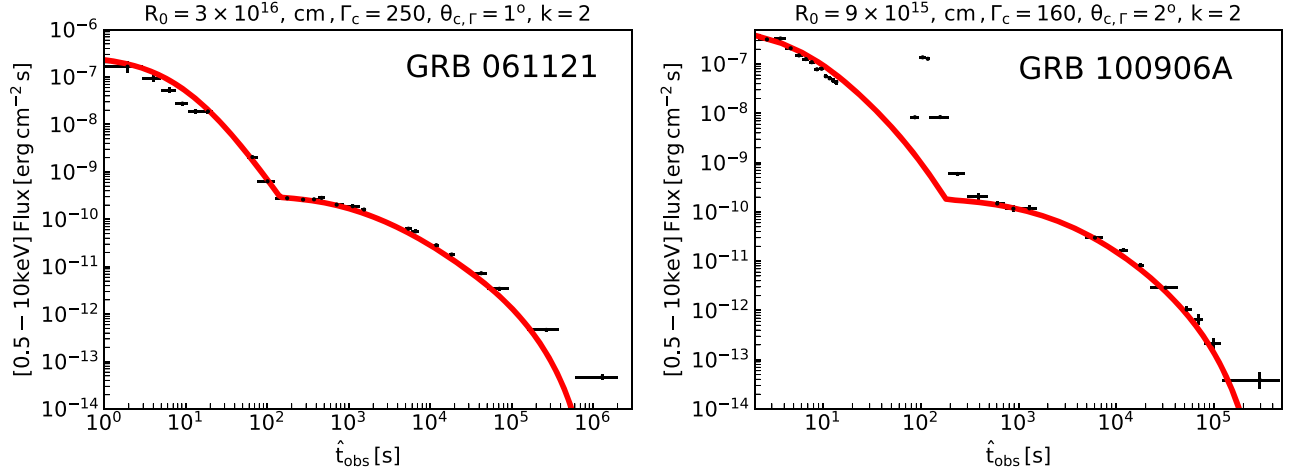


Figure 5. X-ray light curves of GRB 061121 (left panel) and GRB 100906A (right panel) modeled by high-latitude emission with the power-law jet structure (red). To model the X-ray light curve of GRB 061121, we have adopted a power-law jet structure with $\Gamma_c = 250$, $R_0 = 3 \times 10^{16}$ cm, $\theta_c = \theta_\Gamma = 1^\circ$, and $k = 2$. For 100906A, we used $\Gamma_c = 160$, $R_0 = 9 \times 10^{15}$ cm, $\theta_c = \theta_\Gamma = 2^\circ$, and $k = 2$. To accurately account for the steep decay phase, we have implemented the synchrotron-like spectra with the characteristic energies derived from the spectral fits around the peak time preceding the steep decay phase: for GRB 061121, we fixed the E_{break} to 3 keV and $E_{\text{peak}} > 150$ keV, while for GRB 100906A, we fixed E_{peak} to 100 keV and E_{break} to 0.1 keV.

interstellar medium (ISM) material) is geometrically thin. While the model itself can account for off-axis viewing angles, we assume here the observer to be on-axis, consistent with the assumption on the prompt emission phase, which speeds up the computation (since in that case we can exploit the azimuthal symmetry of the afterglow image and thus effectively reduce the EATS dimensionality by one). In order to compute the afterglow emission, we need to specify the jet kinetic energy profile $dE_K/d\Omega(\theta)$. The simplest (and most widely used) assumption, which we adopt here, is to set the energy radiated in the prompt phase from each solid angle element to a constant fraction of the kinetic energy of the jet material.⁹ In our case, this leads (see Appendix A of Salafia et al. 2015) to $dE_K/d\Omega(\theta) \propto \beta^2(\theta)\epsilon(\theta)$. Thus, the angular dependence of the kinetic energy is approximately the same as that of ϵ , namely

$$\frac{dE_K}{d\Omega} = \begin{cases} (E_c/4\pi) & \theta \leq \theta_c \\ (E_c/4\pi)(\theta/\theta_c)^{-k} & \theta > \theta_c \end{cases} \quad (5)$$

in the power-law case, or

$$\frac{dE_K}{d\Omega} = \frac{E_c}{4\pi} \exp\left[-\left(\frac{\theta}{\theta_c}\right)^2\right] \quad (6)$$

in the Gaussian case. Here, E_c is the jet core isotropic-equivalent kinetic energy. The initial Lorentz factor profile is still given by Equation (4). The remaining relevant parameters for the afterglow phase are the external ISM number density n , the shock-accelerated electron power-law index p , the post-shock internal energy density fraction shared by the accelerated electrons ϵ_e , and the fraction shared by the magnetic field ϵ_B , all of which we assume to be independent from the angle.

⁹ While being simple, this assumption actually conflicts with what one would expect, e.g., in the internal shock scenario: slower parts of the jet are presumably less efficient in converting kinetic energy into prompt emission. Accounting for this kind of effect would therefore go in the direction of making the decay in Equation (5) shallower.

3.2.1. GRB 061121

In order to model the multiwavelength emission of the GRB 061121, we collected the optical data in the Swift/UVOT white filter from Page et al. (2007). The observed magnitudes are corrected for the Galactic extinction (Schlafly & Finkbeiner 2011) and for extinction in the host galaxy. We use a model including the high-latitude emission and the forward shock afterglow from the same jet structure. The model with the X-ray and optical observations is shown in Figure 6. We assume a power-law jet structure with $k_E = 2$, $k_\Gamma = 2.2$, $\Gamma_c = 180$, $\theta_c = \theta_\Gamma = 2^\circ$, $E_c = 3 \times 10^{53}$ erg, $n = 0.3$ cm⁻³, $p = 2.1$, $\epsilon_e = 0.1$, and $\epsilon_B = 10^{-4}$. Here, k_E and k_Γ refer to the power-law indices of the energy and Lorentz factor structures, respectively. As described in the previous section, we assume a 2BPL shape for the prompt emission intrinsic spectrum. We fix the comoving peak photon energy at $E'_{\text{peak}} = 500$ keV/ $\Gamma_c = 2.8$ keV, the comoving low-energy break photon energy at $E'_{\text{break}} = 3$ keV/ $\Gamma_c = 1.7 \times 10^{-2}$ keV, the photon indices to $\alpha_1 = -2/3$, $\alpha_2 = -1/2$, and the high-energy photon index to $\beta = -4.1$. Finally, we assume a prompt emission radius $R_0 = 5 \times 10^{15}$ cm, and we assume that the high-latitude emission starts 60 s after the GRB trigger time (i.e., around the time of the main pulse). The resulting high-latitude emission in the X-rays dominates over the forward shock emission during the plateau. It is necessary to produce the initial steep decay in the X-ray and optical bands as well as the flatness and the duration of the X-ray plateau. On the other hand, the resulting predicted high-latitude emission is negligible with respect to the forward shock in the optical band. The high-latitude optical emission is faint because it corresponds to the low-energy tail of the prompt emission spectrum. The high-latitude emission and the forward shock expected from the structured jet are able to explain the chromatic behavior of the optical and X-ray light curves. We also test a Gaussian profile for the jet structure finding almost identical results.

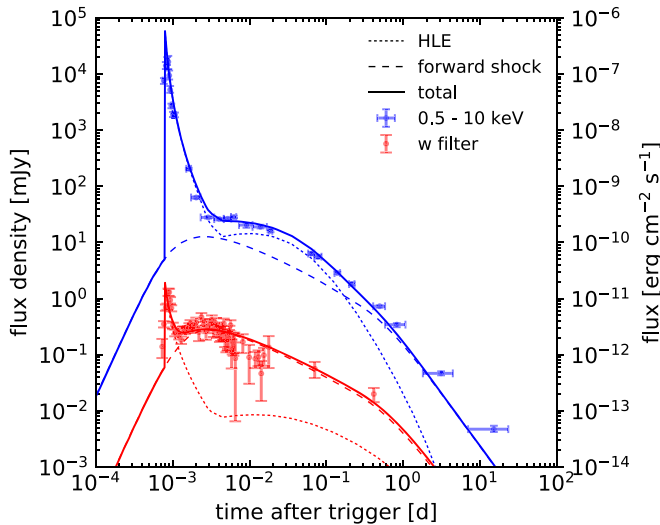


Figure 6. GRB 061121 light curves as observed by XRT (energy flux in the 0.5–10 keV band, blue error bars) and UVOT (mean flux density in the white filter, red error bars, de-reddened assuming $E(B - V) = 0.055$) compared to the predictions of our model (solid lines), where both the high-latitude emission (dotted lines) and forward shock (dashed lines) emission are taken into account. The adopted parameters are reported in the text. The w filter model light curve accounts for the transmission curve of the filter, retrieved from the HEASARC website (<https://heasarc.gsfc.nasa.gov/docs/heasarc/caldb/swift/docs/uvot/>).

3.2.2. GRB 100906A

We collected multi-filter optical data from Gorbvskoy et al. (2012) and A. Melandri (2020, private communication). The observed magnitudes are corrected for galactic extinction (Schlafly & Finkbeiner 2011) and for extinction in the host galaxy. Figure 7 shows the comparison between the observed light curves and our high-latitude and forward shock emission models, obtained assuming a Gaussian jet structure with $\Gamma_c = 160$, $\theta_c = 4^\circ.2$, $\theta_\Gamma = 3^\circ.3$, $E_c = 5 \times 10^{53}$ erg, $n = 15 \text{ cm}^{-3}$, $p = 2.1$, $\epsilon_e = 0.03$, and $\epsilon_B = 2 \times 10^{-2}$. For the prompt emission, we assume again a 2BPL spectrum as before, with parameters taken from spectral fitting of the brightest BAT pulse. Taking the fitting parameters from Oganessian et al. (2017), we obtain $E'_{\text{peak}} = 100 \text{ keV}/\Gamma_c = 0.625 \text{ keV}$, $E'_{\text{break}} = 10 \text{ keV}/\Gamma_c = 6.25 \times 10^{-2} \text{ keV}$, and $\alpha_1 = -2/3$, $\alpha_2 = -1/2$ as before. The high-energy photon index is set to $\beta = -3.2$, and we assume a prompt emission radius $R_0 = 3 \times 10^{15} \text{ cm}$. A second, later emission event with an almost comparable peak flux is present in the XRT light curve at around 100 s post-trigger. The spectrum of this pulse can be fitted by the 2SBPL with $E_{\text{peak}} \sim 5 \text{ keV}$ and $E_{\text{break}} \lesssim 1 \text{ keV}$, with a high-energy spectral slope $\beta \sim -3.7$. Although it is subdominant, given the softer spectrum, we included the high-latitude emission from this pulse for completeness. For this pulse, we adopt the same jet structure of the first one, and we assume a starting time $t_0 = 85 \text{ s}$ in the observer frame. Also in this case, the combination of the high-latitude and forward shock emission is able to explain the features of the multiwavelength light curves (see Figure 7), with the high-latitude emission dominating over the forward shock emission during the plateau phase in the X-rays, while it is negligible in the optical range. Note that we find equally satisfying results with a power-law structure, setting $\theta_c = \theta_\Gamma = 2^\circ$ and using slopes $k_E = 2$ and $k_\Gamma = 3.1$. In this latter case, the structure

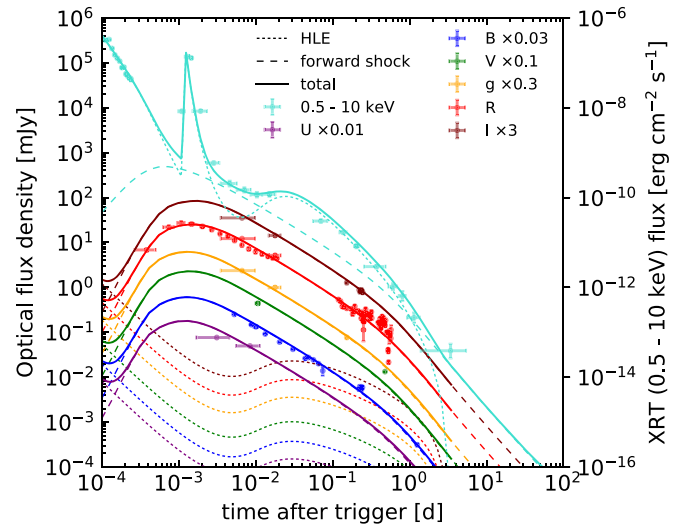


Figure 7. Same as Figure 6 but for GRB 100906A light curves as observed by XRT (energy flux in the 0.5–10 keV band, cyan error bars) and in optical as observed by several facilities (in-band flux density, colored error bars, rescaled for for better visualization by the factors shown in the legend). The adopted parameters are reported in the text.

would be very similar to the one we find for GRB 061121, the differences being almost entirely in the distance and ISM density, pointing to the quasi-universal jet structure hypothesis (Salafia et al. 2015, 2019a, 2019b).

3.3. Spectral Properties of the High-latitude Emission Plateau

Predictions of the high-latitude emission model extend to the spectral properties of GRB X-ray counterparts. Since, in our model, the high-latitude emission gives an essential contribution to the X-ray emission in the plateau phase, we expect that the GRB X-ray spectrum includes properties of the prompt emission spectrum. Assuming that the comoving spectrum is the same at all angles θ , the decrease of \mathcal{D} with time means that the observer is probing a progressively higher energy part of the prompt emission spectrum, since the observed photon energy is $E_{\text{obs}} = E'\mathcal{D}$. For the Gaussian jet structure with $\Gamma_c \sim 100$, our results indicate that $\mathcal{D} \sim 10$ at the start of the plateau. Therefore, the spectral index in the plateau phase (at $\sim 10 \text{ keV}$) would correspond to that at around ~ 100 of keV in the prompt emission pulse at t_0 . This is close to the typical peak energy of the prompt emission spectrum ($\sim 200 \text{ keV}$; e.g., Nava et al. 2011). The photon index in the plateau phase can vary between -1.5 , the spectral slope below E_{peak} , and $\hat{\beta}_p$, which is the photon index above E_{peak} . The value of $\hat{\beta}_p$ ranges between -2 and -3 (e.g., Nava et al. 2011), which is consistent with the spectral analysis of the plateau phase found by Liang et al. (2007), who suggest a range of photon indices between -1.5 and -2.5 .

4. Conclusions

We studied the high-latitude emission arising from a switched-off pulse of relativistic jets with an angular structure in the bulk motion and comoving brightness. Using both Gaussian and power-law jet structures, we tested the predictions of our model by comparing them with the X-ray and optical light curves of the GRB 061121 and GRB 100906A. Our results are summarized as follows:

1. The plateau phase observed in a good fraction of X-ray GRB light curves can arise from the high-latitude emission of a structured jet. Plateaus starting at $t_{\text{obs}} \sim 10^2\text{--}10^3$ s require that the size of the jet at the start of the plateau be $R_0 \gtrsim 10^{15}$ cm. While in the Gaussian jet structure, only plateau durations of $\sim 10^3$ s can be obtained, the power-law jet structure can provide more extended plateaus (up to $\sim \text{few} \times 10^4$ s). However, changing the emission region and jet parameters, the model can account for longer and brighter X-ray plateaus as observed by Swift/XRT.
2. The high-latitude emission model from a structured jet is expected to produce two further segments during the flux decay in the post-plateau phase: a power-law followed by a very sharp drop. The sharp drop can provide a novel explanation for such puzzling features observed in some GRB X-ray light curves (e.g., Troja et al. 2007).
3. Adding the high-latitude emission to the radiation from the forward shock enables us to account for the chromatic behavior of the light curves in the optical and X-ray bands. This is mainly due to the interplay between the two separated emission regions: the X-ray plateau comes from the prompt emitting wings of the jet while the optical is most likely dominated by forward shock emission.
4. The spectra of the plateau phase in the X-ray energy range are consistent with the high-latitude emission predictions. In particular, measured photon indices ($-2.5 < \alpha < -1.5$; Liang et al. 2007) are in agreement with the synchrotron model for the prompt emission. The spectral softening typically observed in the steep-decay/plateau transition is also naturally explained in our model.

Previous studies of high-latitude emission from inhomogeneous jets (Dyks et al. 2005; Yamazaki et al. 2006; Takami et al. 2007) were focused on the influence of jet structure on the fast decay phase. The flattening of high-latitude emission at ~ 30 s due to the bulk motion structure has been noticed previously in Dyks et al. (2005). However, these authors did not obtain results for the plateau phase observed at $\sim 10^2\text{--}10^3$ s. This is due to the limited parameter space considered in their work, e.g., the size of the jet, fixed to $R_0 \sim 10^{14}$ cm.

Here, we have shown that the high-latitude emission from a structured jet is able to explain the complex morphology of X-ray counterparts of GRBs, including fast decay, plateau, and post-plateau phases. The high-latitude emission added to radiation from the forward shock is able to produce the shape, the luminosity, and the duration of the X-ray emission and to account for the chromatic behavior of the X-ray/optical light curves. The systematic application of this model to optical-to-X-ray data will provide a means of probing the angular structure of GRB jets and the size of the emitting region during prompt emission. A thorough exploration of these aspects will be the subject of subsequent works.

We would like to thank Andrea Melandri for sharing the optical data. G.O. is thankful to Gabriele Ghisellini and Elias S. Kammoun for fruitful discussions. M.B., S.D.O., and G.O. acknowledge financial contribution from the agreement ASI-INAF n.2017-14-H.0. G.O. and S.A. are thankful to INAF—Osservatorio Astronomico di Brera for kind hospitality during the completion of this work. S.A. acknowledges the GRAvitational Wave Inaf TeAm—GRAWITA (P.I. E. Brocato) and the

PRIN-INAF “Toward the SKA and CTA era: discovery, localization and physics of transient sources.” This work made use of data supplied by the UK Swift Science Data Centre at the University of Leicester.

Appendix Light Curve of the High-latitude Emission from a Structured Outflow

The observed specific flux of the source is defined in the following way:

$$F_\nu = \int d\Omega_{\text{obs}} I_\nu(\nu, t) \cos(\theta_{\text{obs}}) \quad (\text{A1})$$

where Ω_{obs} , I_ν , and θ_{obs} are the observed solid angle, the observed specific intensity, and the angle between the normal of the observing surface of the instrument and the element of the surface from where the photons come.

We further assume the object of our interest, i.e., an instantaneous emission produced throughout a structured outflow at a given time. Due to the infinitesimally short duration of the pulse, at a given time, the observer receives the emission from a certain equal arrival time ring from the surface of the outflow. Therefore, given that the specific intensity in the lab frame transforms like $I_\nu(\nu, t) = D^3(\theta) I'_{\nu'}(\nu', t)$, the general Equation (A1) for an observer aligned with the center of the outflow returns

$$F_\nu(t_{\text{obs}}) = \frac{2\pi}{d_L^2} \int_0^{\pi/2} \eta'_{\nu'}(\nu') \delta(t - t_{\text{em}}) \times D^3(\theta) R^2(\theta) \sin \theta \cos \theta d\theta \quad (\text{A2})$$

where d_L is the luminosity distance to the source, and $R(\theta)$ is the radius of the outflow measured from its origin. We wrote the specific intensity in the comoving frame as $I'_{\nu'}(\nu', t) = \eta'_{\nu'}(\nu') \delta(t - t_{\text{em}})$, where $\eta'_{\nu'}$ is the energy emitted per unit area, per unit frequency, per unit solid angle, at an angle θ , as measured in the comoving frame, and $\delta(t - t_{\text{em}})$ is the Dirac delta function. At a given time t_{em} measured in the lab frame, the infinitesimally short-duration pulse is produced throughout the entire outflow with the same spectral shape $S(\nu')$. At an observer time $t_{\text{obs}} = t[1 - \beta(\theta) \cos \theta] = t/D(\theta)\Gamma(\theta)$, the specific flux is given by

$$F_\nu(t_{\text{obs}}) = \frac{2\pi}{d_L^2} \frac{1}{t_{\text{obs}}} \int_0^{\pi/2} \eta'_{\nu'}(\nu') D^3(\theta) \times \frac{\delta(\theta - \theta_{\text{obs}})}{D^2(\theta_{\text{obs}}) \Gamma^2(\theta_{\text{obs}}) \left| \frac{d\beta}{d\theta} \cos \theta - \beta \sin \theta \right|_{\theta=\theta(t_{\text{obs}})}} \times R^2(\theta) \sin \theta \cos \theta d\theta \quad (\text{A3})$$

where we applied the following transformation for the Dirac delta (which corresponds to the standard transformation rule for the Dirac delta of a function):

$$\delta(t - t_{\text{em}}) = \delta[t_{\text{obs}} D(\theta) \Gamma(\theta) - t_{\text{em}}] = \frac{\delta(\theta - \theta_{\text{obs}})}{\left| \frac{d}{d\theta} [t_{\text{obs}} D(\theta) \Gamma(\theta) - t_{\text{em}}] \right|_{\theta=\theta(t_{\text{obs}})}} \quad (\text{A4})$$

where $\theta(t_{\text{obs}})$ is the angle where the photons reaching the observer at a given t_{obs} are emitted from (which corresponds to

the solution of $t_{\text{obs}}D(\theta)\Gamma(\theta) = t_{\text{em}}$. The derivative at the denominator can be written explicitly as

$$\begin{aligned} \frac{d}{d\theta}[t_{\text{obs}}D(\theta)\Gamma(\theta) - t_{\text{em}}] &= t_{\text{obs}} \frac{d}{d\theta}[D(\theta)\Gamma(\theta)] \\ &= t_{\text{obs}}D^2\Gamma^2 \left(\frac{d\beta}{d\theta} \cos \theta - \beta \sin \theta \right). \end{aligned} \quad (\text{A5})$$

With the aid of Dirac delta, the solution of the integral in Equation (A3) is straightforward and is written as

$$\begin{aligned} F_\nu(t_{\text{obs}}) &= \frac{2\pi R_0^2 D^2(\theta(t_{\text{obs}})) \eta'_{\nu'}(\nu')}{d_L^2 \beta_0^2 \Gamma(\theta(t_{\text{obs}}))} \\ &\times \frac{\beta^2(\theta(t_{\text{obs}})) \sin \theta(t_{\text{obs}}) \cos \theta(t_{\text{obs}})}{t_{\text{obs}}D(\theta(t_{\text{obs}}))\Gamma(\theta(t_{\text{obs}})) \left| \frac{d\beta}{d\theta} \cos \theta - \beta \sin \theta \right|_{\theta=\theta(t_{\text{obs}})}} \end{aligned} \quad (\text{A6})$$

where we used $R(\theta(t_{\text{obs}})) = R_0\beta(\theta(t_{\text{obs}}))/\beta_0$.

We can further simplify Equation (A6) by noticing that

$$\begin{aligned} \frac{d\theta}{dt_{\text{obs}}} &= - \frac{1}{t_{\text{em}} \left(\frac{d\beta}{d\theta} \cos \theta - \beta \sin \theta \right)} \\ &= \frac{1}{t_{\text{obs}}D(\theta)\Gamma(\theta) \left| \frac{d\beta}{d\theta} \cos \theta - \beta \sin \theta \right|}. \end{aligned} \quad (\text{A7})$$

This equation is obtained from $t_{\text{obs}}D(\theta)\Gamma(\theta) = t_{\text{em}}$. Considering that $\beta(\theta)$ is decreasing with θ , the argument of the module at the denominator is negatively defined.

Substituting this last equation into (A6), we obtain

$$\begin{aligned} F_\nu(t_{\text{obs}}) &= \frac{2\pi R_0^2}{d_L^2 \beta_0^2} (D^2(\theta) S(\nu')) \\ &\times \epsilon(\theta) \left. \frac{\beta^2(\theta)}{\Gamma(\theta)} \cos \theta \sin \theta \frac{d\theta}{dt_{\text{obs}}} \right)_{\theta=\theta(t_{\text{obs}})}. \end{aligned} \quad (\text{A8})$$

We have introduced the angular dependence of the comoving brightness, i.e., we set $\eta'_{\nu'} = \epsilon(\theta)S(\nu')$. We also used Equation (1) to simplify the final expression and to represent it in terms of the differential area $\sin\theta d\theta/dt_{\text{obs}}$. The observed time t_{obs} is measured from the imaginary photon emitted at $R = 0$. However, one can easily change the reference time to the time at R_0 by introducing a delay of $R_0/c[1/\beta(0) - 1]$. It is worth noticing that the delta function that appears in I'_ν is defined in the lab frame. This is the proper frame to define an instantaneous emission. It can be expressed as a delta function in the comoving frame $\delta(t - t_{\text{em}}) = \Gamma(\theta)\delta(t' - t'_{\text{em}})$, where $t' - t'_{\text{em}} = \Gamma(\theta)(t - t_{\text{em}})$ is the time interval in the comoving frame. By repeating all of the previous calculations with this expression leads to the same expressions of Equation (A8).

In order to make this as explicit as possible, we show the dependence of Equation (A8) on t_{obs} . To this aim, noticing that $D(\theta(t_{\text{obs}})) = t_{\text{em}}/(t_{\text{obs}}\Gamma(\theta(t_{\text{obs}})))$ and $t_{\text{em}} = R_0/(\beta_0c)$, we can

write

$$\begin{aligned} F_\nu(t_{\text{obs}}) &= \frac{2\pi R_0^4}{d_L^2 \beta_0^4 c^2} (S(\nu') \epsilon(\theta)) \\ &\times \left. \frac{\beta^2(\theta)}{\Gamma^3(\theta)} \cos \theta \sin \theta \frac{d\theta}{dt_{\text{obs}}} \right)_{\theta=\theta(t_{\text{obs}})} t_{\text{obs}}^{-2}. \end{aligned} \quad (\text{A9})$$

If we consider a power-law spectrum $S_{\nu'} = S_{\nu'_0} \nu'^{\beta_s} \nu'^{-\beta_s}$, where β_s is the spectral index, the general equation Equation (A9) becomes

$$\begin{aligned} F_\nu(t_{\text{obs}}) &= \frac{2\pi R_0^2}{d_L^2 \beta_0^2} \left(\frac{R_0}{\beta_0 c} \right)^{2+\beta_s} S_{\nu'_0} \nu'^{\beta_s} \\ &\times \left(\epsilon(\theta) \frac{\beta^2(\theta)}{\Gamma^{3+\beta_s}(\theta)} \cos \theta \sin \theta \frac{d\theta}{dt_{\text{obs}}} \right)_{\theta=\theta(t_{\text{obs}})} \nu^{-\beta_s} t_{\text{obs}}^{-(2+\beta_s)}. \end{aligned} \quad (\text{A10})$$

This last equation shows the power-law temporal behavior of Kumar & Panaitescu (2000; see also Uhm & Zhang 2015 and Kumar & Zhang 2015), but there is a further time-dependent factor that comes from the structure of the jet, and it is dependent on θ in Equation (A10). The solution of Kumar & Panaitescu (2000) is thus recovered in the spherical case (setting $\epsilon(\theta) = 1$ and $\cos \theta(t_{\text{obs}}) \simeq 1$):

$$F_\nu(t_{\text{obs}}) = \frac{2\pi R_0}{d_L^2} \left(\frac{R_0}{\beta_0 c} \right)^{2+\beta_s} S_{\nu'_0} \nu'^{\beta_s} \frac{c}{\Gamma^{3+\beta_s}} \nu^{-\beta_s} t_{\text{obs}}^{-(2+\beta_s)}. \quad (\text{A11})$$

ORCID iDs

Gor Oganesyan  <https://orcid.org/0000-0001-9765-1552>
Stefano Ascenzi  <https://orcid.org/0000-0001-5116-6789>
Marica Branchesi  <https://orcid.org/0000-0003-1643-0526>
Om Sharan Salafia  <https://orcid.org/0000-0003-4924-7322>

References

- Barthelmy, S. D., Baumgartner, W. H., Cummings, J. R., et al. 2010, *GCN*, 11233, 1
- Beniamini, P., Barniol Duran, R., & Giannios, D. 2018, *MNRAS*, 476, 1785
- Beniamini, P., & Mochkovitch, R. 2017, *A&A*, 605, A60
- Beniamini, P., & Nakar, E. 2019, *MNRAS*, 482, 5430
- Beniamini, P., & Piran, T. 2013, *ApJ*, 769, 69
- Blandford, R. D., & McKee, C. F. 1976, *PhFl*, 19, 1130
- Cannizzo, J. K., & Gehrels, N. 2009, *ApJ*, 700, 1047
- Dai, Z. G. 2004, *ApJ*, 606, 1000
- Dai, Z. G., & Gou, L. J. 2001, *ApJ*, 552, 72
- Dai, Z. G., & Lu, T. 1998a, *A&A*, 333, L87
- Dai, Z. G., & Lu, T. 1998b, *PhRvL*, 81, 4301
- Daigne, F., & Mochkovitch, R. 1998, *MNRAS*, 296, 275
- Dall'Osso, S., Stratta, G., Guetta, D., et al. 2011, *A&A*, 526, A121
- Dermer, C. D. 2004, *ApJ*, 614, 284
- Duffell, P. C., & MacFadyen, A. I. 2015, *ApJ*, 806, 205
- Dyks, J., Zhang, B., & Fan, Y. Z. 2005, arXiv:astro-ph/0511699
- Eichler, D., & Granot, J. 2006, *ApJL*, 641, L5
- Fan, Y., & Piran, T. 2006, *MNRAS*, 369, 197
- Fenimore, E. E., Madras, C. D., & Nayakshin, S. 1996, *ApJ*, 473, 998
- Gehrels, N., Chincarini, G., Giommi, P., et al. 2004, *ApJ*, 611, 1005
- Genet, F., Daigne, F., & Mochkovitch, R. 2007, *MNRAS*, 381, 732
- Genet, F., & Granot, J. 2009, *MNRAS*, 399, 1328
- Ghirlanda, G., Salafia, O. S., Paragi, Z., et al. 2019, *Sci*, 363, 968
- Ghirlandini, G., Ghirlanda, G., Nava, L., & Firmani, C. 2007, *ApJL*, 658, L75
- Golenetskii, S., Aptekar, R., Frederiks, D., et al. 2010, *GCN*, 11251, 1
- Golenetskii, S., Aptekar, R., Mazets, E., et al. 2006, *GCN*, 5837, 1

- Gorbovskey, E. S., Lipunova, G. V., Lipunov, V. M., et al. 2012, *MNRAS*, **421**, 1874
- Granot, J., & Kumar, P. 2006, *MNRAS*, **366**, L13
- Ioka, K., Toma, K., Yamazaki, R., & Nakamura, T. 2006, *A&A*, **458**, 7
- Jin, Z. P., Yan, T., Fan, Y. Z., & Wei, D. M. 2007, *ApJL*, **656**, L57
- Kalberla, P. M. W., Burton, W. B., Hartmann, D., et al. 2005, *A&A*, **440**, 775
- Katz, J. I. 1994, *ApJL*, **432**, L107
- Kobayashi, S., Piran, T., & Sari, R. 1997, *ApJ*, **490**, 92
- Kobayashi, S., & Zhang, B. 2007, *ApJ*, **655**, 973
- Kumar, P., & McMahon, E. 2008, *MNRAS*, **384**, 33
- Kumar, P., & Panaitescu, A. 2000, *ApJL*, **541**, L51
- Kumar, P., & Zhang, B. 2015, *PhR*, **561**, 1
- Leventis, K., Wijers, R. A. M. J., & van der Horst, A. J. 2014, *MNRAS*, **437**, 2448
- Li, L., Wu, X.-F., Huang, Y.-F., et al. 2015, *ApJ*, **805**, 13
- Liang, E. W., Zhang, B., O'Brien, P. T., et al. 2006, *ApJ*, **646**, 351
- Liang, E.-W., Zhang, B.-B., & Zhang, B. 2007, *ApJ*, **670**, 565
- Lin, D.-B., Liu, T., Lin, J., et al. 2018, *ApJ*, **856**, 90
- Lindner, C. C., Milosavljević, M., Couch, S. M., & Kumar, P. 2010, *ApJ*, **713**, 800
- Lipunov, V. M., Postnov, K. A., & Prokhorov, M. E. 2001, *ARep*, **45**, 236
- Lloyd, N. M., & Petrosian, V. 2000, *ApJ*, **543**, 722
- Markwardt, C. B., Barthelmy, S. D., Beardmore, A. P., et al. 2010, *GCN*, **11227**, 1
- Meszáros, P., & Rees, M. J. 1993, *ApJ*, **405**, 278
- Meszáros, P., & Rees, M. J. 1997, *ApJ*, **476**, 232
- Metzger, B. D., Giannios, D., Thompson, T. A., Bucciantini, N., & Quataert, E. 2011, *MNRAS*, **413**, 2031
- Nava, L., Ghirlanda, G., Ghisellini, G., & Celotti, A. 2011, *A&A*, **530**, A21
- Nousek, J. A., Kouveliotou, C., Grupe, D., et al. 2006, *ApJ*, **642**, 389
- O'Brien, P. T., Willingale, R., Osborne, J., et al. 2006, *ApJ*, **647**, 1213
- Oganesyan, G., Nava, L., Ghirlanda, G., & Celotti, A. 2017, *ApJ*, **846**, 137
- Oganesyan, G., Nava, L., Ghirlanda, G., & Celotti, A. 2018, *A&A*, **616**, A138
- Oganesyan, G., Nava, L., Ghirlanda, G., Melandri, A., & Celotti, A. 2019, *A&A*, **628**, A59
- Page, K. L., Barthelmy, S. D., Beardmore, A. P., et al. 2006, *GCN*, **5823**, 1
- Page, K. L., Willingale, R., Osborne, J. P., et al. 2007, *ApJ*, **663**, 1125
- Pescalli, A., Ghirlanda, G., Salafia, O. S., et al. 2015, *MNRAS*, **447**, 1911
- Qin, Y. P. 2008, *ApJ*, **683**, 900
- Ravasio, M. E., Ghirlanda, G., Nava, L., & Ghisellini, G. 2019, *A&A*, **625**, A60
- Ravasio, M. E., Oganesyan, G., Ghirlanda, G., et al. 2018, *A&A*, **613**, A16
- Rees, M. J., & Meszáros, P. 1994, *ApJL*, **430**, L93
- Rees, M. J., & Mészáros, P. 1998, *ApJL*, **496**, L1
- Rossi, E., Lazzati, D., & Rees, M. J. 2002, *MNRAS*, **332**, 945
- Salafia, O. S., Barbieri, C., Ascenzi, S., & Toffano, M. 2019a, arXiv:1907.07599
- Salafia, O. S., Ghirlanda, G., Ascenzi, S., & Ghisellini, G. 2019b, *A&A*, **628**, A18
- Salafia, O. S., Ghisellini, G., Pescalli, A., Ghirlanda, G., & Nappo, F. 2015, *MNRAS*, **450**, 3549
- Salafia, O. S., Ghisellini, G., Pescalli, A., Ghirlanda, G., & Nappo, F. 2016, *MNRAS*, **461**, 3607
- Sari, R., & Piran, T. 1997, *MNRAS*, **287**, 110
- Sari, R., Piran, T., & Narayan, R. 1998, *ApJL*, **497**, L17
- Schlafly, E. F., & Finkbeiner, D. P. 2011, *ApJ*, **737**, 103
- Shao, L., & Dai, Z. G. 2007, *ApJ*, **660**, 1319
- Tagliaferri, G., Goad, M., Chincarini, G., et al. 2005, *Natur*, **436**, 985
- Takami, K., Yamazaki, R., Sakamoto, T., & Sato, G. 2007, *ApJ*, **663**, 1118
- Tavani, M. 1996, *ApJ*, **466**, 768
- Toma, K., Ioka, K., Yamazaki, R., & Nakamura, T. 2006, *ApJL*, **640**, L139
- Troja, E., Cusumano, G., O'Brien, P. T., et al. 2007, *ApJ*, **665**, 599
- Uhm, Z. L., & Beloborodov, A. M. 2007, *ApJL*, **665**, L93
- Uhm, Z. L., & Zhang, B. 2015, *ApJ*, **808**, 33
- Willingale, R., O'Brien, P. T., Osborne, J. P., et al. 2007, *ApJ*, **662**, 1093
- Wilms, J., Allen, A., & McCray, R. 2000, *ApJ*, **542**, 914
- Yamazaki, R. 2009, *ApJL*, **690**, L118
- Yamazaki, R., Toma, K., Ioka, K., & Nakamura, T. 2006, *MNRAS*, **369**, 311
- Yu, Y.-W., Cheng, K. S., & Cao, X.-F. 2010, *ApJ*, **715**, 477
- Zhang, B., Fan, Y. Z., Dyks, J., et al. 2006, *ApJ*, **642**, 354
- Zhang, B., & Mészáros, P. 2001, *ApJL*, **552**, L35
- Zhang, B., & Mészáros, P. 2002, *ApJ*, **571**, 876
- Zhang, B.-B., Uhm, Z. L., Connaughton, V., Briggs, M. S., & Zhang, B. 2016, *ApJ*, **816**, 72
- Zhang, B. B., Zhang, B., Castro-Tirado, A. J., et al. 2018, *NatAs*, **2**, 69
- Zhang, B.-B., Zhang, B., Liang, E.-W., & Wang, X.-Y. 2009, *ApJL*, **690**, L10